



HAL
open science

Tomography Imaging of Lithium Electrodeposits Using Neutron, Synchrotron X-ray, and Laboratory X-ray sources: A Comparison

Lucile Magnier, Lauréline Lecarme, Fannie Alloin, Andrew King, Renaud Bouchet, Alessandro Tengattini, Didier Devaux, Eric Maire

► To cite this version:

Lucile Magnier, Lauréline Lecarme, Fannie Alloin, Andrew King, Renaud Bouchet, et al.. Tomography Imaging of Lithium Electrodeposits Using Neutron, Synchrotron X-ray, and Laboratory X-ray sources: A Comparison. *Frontiers in Energy Research*, 2021, 9, 10.3389/fenrg.2021.657712 . hal-03262977

HAL Id: hal-03262977

<https://hal.science/hal-03262977>

Submitted on 16 Jun 2021

HAL is a multi-disciplinary open access archive for the deposit and dissemination of scientific research documents, whether they are published or not. The documents may come from teaching and research institutions in France or abroad, or from public or private research centers.

L'archive ouverte pluridisciplinaire **HAL**, est destinée au dépôt et à la diffusion de documents scientifiques de niveau recherche, publiés ou non, émanant des établissements d'enseignement et de recherche français ou étrangers, des laboratoires publics ou privés.

1 Tomography Imaging of Lithium Electrodeposits Using Neutron, 2 Synchrotron X-ray, and Laboratory X-ray sources: A Comparison.

3 Lucile Magnier^{1,2}, Lauréline Lecarme¹, Fannie Alloin^{1,3}, Eric Maire², Andrew King⁴, Renaud
4 Bouchet¹, Alessandro Tengattini^{5,6}, Didier Devaux^{1,3,**}

5 ¹Univ. Grenoble Alpes, Univ. Savoie Mont Blanc, CNRS, Grenoble INP*, LEPMI, 38000 Grenoble,
6 France

7 ²Univ Lyon, INSA Lyon, CNRS UMR 5510, MATEIS, 69621 Villeurbanne, France

8 ³Réseau sur le Stockage Electrochimique de l'Energie (RS2E), CNRS, FR3459, 80 039 Amiens
9 Cedex, France

10 ⁴Synchrotron Soleil, Psiché beamline, 91190 Gif-sur-Yvette, France

11 ⁵Univ. Grenoble Alpes, CNRS, Grenoble INP*, 3SR, 38000 Grenoble, France

12 ⁶Institut Laue-Langevin (ILL), 71 Avenue des Martyrs, 38000 Grenoble, France

13 *Institute of Engineering and Management Univ. Grenoble Alpes

14

15 **** Correspondence :**

16 Didier Devaux

17 didier.devaux@grenoble-inp.fr

18 **Keywords: lithium metal, electrodeposit, dendrite, neutron tomography, X-ray tomography,**
19 **synchrotron**

20 **Abstract**

21 X-ray and neutron imaging are widely employed for battery materials thanks to the possibility to
22 perform non-invasive *in situ* and *in operando* analyses. X-ray tomography can be performed either in
23 synchrotron or laboratory facilities and is particularly well-suited to analyze bulk materials and
24 electrode/electrolyte interfaces. Several post Lithium-ion (Li-ion) devices, such as Li-sulfur, Li-O₂, or
25 all-solid-state Li batteries, have in common an anode made of metallic Li. The main failure mode of
26 Li batteries is the inhomogeneity of the Li electrodeposits onto the Li anode during charge steps leading
27 to dendrite growth and low Coulombic efficiency. X-ray tomography is a powerful tool to study
28 dendrites as it provides useful information about their locations, dynamics, and microstructures. So far,
29 the use of neutron tomography is scarcely reported for Li deposit analysis due to the difficulty to reach
30 sufficient image resolution to capture the deposit microstructure, *i.e.* typically below 10-20 μm. The
31 very different interactions of X-rays and neutrons with Li, which has significantly different opacity in
32 the two cases, make the two techniques highly complementary. Notably, the capacity of neutrons to
33 discern different Li isotopes is pivotal to get an insight on the composition of Li deposits by

34 distinguishing between Li originating from an electrode (${}^6\text{Li}$ in this study) to that from the Li salt
35 electrolyte (mainly in ${}^7\text{Li}$ here). Indeed, the theoretical linear neutron attenuation coefficient of ${}^6\text{Li}$ is
36 about 15 and 2000 larger than that of natural Li and ${}^7\text{Li}$, respectively. Therefore, high imaging contrast
37 difference is obtained between ${}^6\text{Li}$ (high attenuation) and natural Li and ${}^7\text{Li}$ (lower attenuations) which
38 could allow a better understanding of the origin of the Li comprising the electrodeposits. In this work,
39 we report, as a proof-of-concept, an *in situ* neutron tomography imaging of Li electrodeposits in a
40 cycled Li symmetric cell. The electrochemical cell comprises a natural Li electrode, a ${}^6\text{Li}$ electrode,
41 and a deuterated liquid electrolyte. The neutron tomographies are compared with X-ray tomography
42 images of the same electrochemical cell acquired both at an X-ray synchrotron beamline and at a
43 laboratory X-ray tomograph. Neutron tomography is shown to be compatible with *in situ* analysis and
44 capable to capture the overall morphology of the Li deposits in good accordance with X-ray
45 tomography analyses.

46 1 Introduction

47 In the journey to develop safe high energy density batteries many systems are currently studied
48 such as Li-sulfur, Li-O₂, or all-solid-state Li devices (Whittingham 2004; W. Li, Song, and Manthiram
49 2017; Bruce et al. 2012). A common feature for those batteries is the use of a lithium (Li) metal negative
50 electrode. Indeed, Li metal is one of the most promising electrode materials thanks to its high capacity
51 (3860 mAh.g⁻¹), low density (0.534 g.cm⁻³), and low electrochemical potential (-3.04 V vs. standard
52 hydrogen electrode) (X.-B. Cheng et al. 2017a). The industrialization of Li metal electrodes with a
53 conventional liquid electrolyte has been hindered by the heterogeneities of the Li electrodeposit onto
54 the Li surface, which limits the Coulombic efficiency (ratio between the discharge and charge
55 capacity), battery cycle life, and may grow sufficiently in the form of dendrite to induce a short-circuit
56 (Aurbach et al. 2000; Z. Li et al. 2014).

57 To move toward an optimized Li-electrolyte interface, understanding the origin and growth of
58 dendrites is of the utmost importance (Z. Li et al. 2014b). Indeed, depending on the nature of the
59 electrolyte and the passive layers (X. B. Cheng et al. 2016a). formed onto the Li metal, different
60 families of dendrite morphologies are observed such as mosses, needles, and globules (Harry et al.
61 2014; K. N. Wood et al. 2016; X.-B. Cheng et al. 2017). Furthermore, the dendrite microstructure
62 depends on the operating and cycling conditions such as temperature or current density (Bai et al.
63 2016a).

64 The most usual techniques to study dendrites are based on optical microscopy (Brissot et al.
65 1999a), electron microscopy (Gireaud et al. 2006), atomic force microscopy (Morigaki and Ohta 1998),
66 or magnetic resonance imaging (Illott et al. 2016) to name a few. However, most of them are two-
67 dimensional and invasive by nature and may alter the probed materials and interfaces. Non-invasive
68 technique based on X-ray imaging which takes advantage of the prevalent interaction of X-ray with
69 the outer electron shell of the atoms are now more accessible thanks to the development of dedicated
70 synchrotron X-ray beamlines and widespread diffusion of laboratory tomographs (Maire et al. 2001;
71 Pietsch and Wood 2017). X-ray tomography is well-suited to study, qualitatively and quantitatively,
72 soft material interfaces. As an example, Balsara *et al.* studied model Li symmetric cells and Li based
73 batteries using synchrotron hard X-ray to report on dendrite growth and volume (Devaux et al. 2015;

74 Harry et al. 2014b). Therefore, X-ray tomography is widely reported to study battery materials (V.
75 Wood 2018; Vanpeene et al. 2020; Magnier et al. 2020). In addition, the temporal and spatial resolution
76 obtained from synchrotron sources are high enough to be compatible with electrochemical processes
77 leading to the development of *in operando* imaging via dedicated electrochemical cells (Schröder et
78 al. 2016; Grey and Tarascon 2017; Sun et al. 2016; Foroozan, Sharifi-Asl, and Shahbazian-Yassar
79 2020).

80 Despite the high spatial and temporal resolution of X-ray imaging techniques, some limitations
81 arise due to the low sensitivity towards light Li compared to materials with high atomic number atoms
82 typically encountered in current collectors (Al, Cu) or active materials (Co, Fe, Mn, Ni). As a
83 complementary non-invasive technique, neutron imaging, which is based on the specific interactions
84 of atomic nuclei with a neutron beam, gives useful additional information thanks to a high penetration
85 depth capability into materials comprising high atomic number elements as well as high Li visibility
86 and sensitivity to its isotopes (Strobl et al. 2009; Banhart et al. 2010). The theoretical linear neutron
87 attenuation coefficient comprising of ^6Li is about 15 and 2000 times larger than that of natural Li and
88 ^7Li , respectively (Sears 1992). As an example of *in operando* neutron radiography, Wang *et al.* imaged
89 at a 50 μm resolution a planar battery made of a highly oriented pyrolytic graphite electrode and ^6Li as
90 counter electrode (Wang et al. 2012). By taking advantage of the beam attenuation induced by ^6Li
91 atoms, the graphite electrode areas enriched with ^6Li were followed over the course of a galvanostatic
92 experiment.

93 Neutron tomography was first applied to commercial batteries to either quantify gas in an alkaline
94 cell or to probe the internal volume modification of battery cell upon cycling (Manke et al. 2007; Butler
95 et al. 2011; Senyshyn et al. 2012). So far, neutron tomography remains an *ex situ* and *in situ* technique
96 as multiple hours are needed to perform a sample acquisition. The Li spatial distribution is typically
97 quantified within cathode (Nanda et al. 2012; Ziesche, Arlt, et al. 2020), anode (Zhang et al. 2017),
98 and battery cell (Ziesche, Robinson, et al. 2020) by neutron tomography. Riley *et al.* performed *in situ*
99 neutron tomography at a 150 μm resolution to report on the jellyroll volume change in Li primary cell
100 (Riley, Hussey, and Jacobson 2010). To get better quantitative data several optimization strategies were
101 proposed by the authors such as designing specific electrochemical cell comprising deuterated
102 electrolytes and isotope enriched Li electrodes. Indeed, ^6Li and ^7Li are strongly attenuating and almost
103 transparent to the neutron beam, respectively.

104 To get specific information within a battery by neutron imaging, dedicated cells and setups
105 (Owejan et al. 2012) are thus needed to increase the spatial and temporal resolution, *i.e.* get information
106 in times compatible with typical beamtime allocations to move toward *in operando* analysis. Several
107 strategies have already been explored such as an electrochemical cell casing made of a neutron
108 transparent polytetrafluoroethylene (PTFE) casing (Owejan et al. 2012), an adapted pouch bag cell
109 (Knoche et al. 2016), or a coin cell (Sun et al. 2017).

110 To combine X-ray and neutron information, Sun *et al.* designed a cylindrical polyamide-imide
111 cell casing having an inner and outer diameter of 3 mm and 6 mm, respectively. The cell is optimized
112 to image Li-air batteries for *in operando* synchrotron X-ray ($\sim 1.2 \mu\text{m}$ resolution) and *in situ* neutron
113 ($\sim 13 \mu\text{m}$ resolution) tomography experiments (Sun et al. 2019). The complementarity of the two
114 techniques revealed the degradation mechanisms at play at the Li/separator interface. Moreover, Song

115 *et al.* (Song et al. 2019) performed *in operando* neutron radiography and *in situ* tomography on a
116 Li/LiMn₂O₄ battery using a TiZr based cell to study the Li dynamic distribution upon dendrite short-
117 circuit. The electrochemically active assembly was made of a neutron transparent ⁷Li metal and
118 deuterated electrolyte in order to enhance the contrast between the Li electrodeposits and the ⁷Li
119 electrode and to reduce the scattering of hydrogen, respectively.

120 In this work, by taking advantage of the capability of a neutron imaging beamline and of the Li
121 isotope sensitivity, we report an *in situ* neutron tomography analysis of Li electrodeposits. A Swagelok-
122 type electrochemical cell with a PTFE casing specifically designed for neutron imaging comprises a
123 Li symmetric cell made of a natural Li (92.4 wt.% ⁷Li and 7.6 wt.% ⁶Li) electrode, a ⁶Li (95 wt.% ⁶Li
124 and 5 wt.% ⁷Li) electrode, and a deuterated liquid electrolyte. ⁶Li was selected to increase the contrast
125 of the deposits from the deuterated electrolyte. The ⁶Li electrode (anode) was oxidized and ⁶Li was
126 plated onto the opposite natural Li electrode (cathode) to induce dendrite growth. The neutron images
127 are then compared to X-ray tomography analysis of the same cell acquired both at an X-ray synchrotron
128 beamline and in a laboratory X-ray tomograph with a voxel size of 0.64 and 2.0 μm, respectively. In
129 addition, the deposit volume is here quantified and positively compares to the measurement obtained
130 by X-ray techniques. Despite the needed optimization to get further image quality and accelerated
131 acquisition time, this *in situ* neutron tomography experiment is a proof-of-concept showing the
132 possibility to study battery failure modes via neutron imaging.

133 2 Material and Methods

134 2.1. Li symmetric cell assembly

135 To minimize neutron or X-ray absorption of the casing, a dedicated electrochemical cell was
136 developed. **Figure S1** (see supplementary file) shows a schematic of the electrochemical cell
137 comprising, as main components, a casing made of polytetrafluoroethylene (PTFE) and current
138 collectors in aluminum (Al). The active cell composed of the ⁶Li/electrolyte/Li assembly is located in
139 its middle. PTFE was selected for its high neutron transparency, allowed by its macromolecular
140 structure made of fluorine and carbon atoms, which have a small neutron cross section. In addition,
141 PTFE based electrochemical cells are known to be suitable for X-ray based techniques (Tan et al.
142 2018). A PTFE Swagelok straight union with a 1/8 inch (~ 3.18 mm) inner diameter was selected to
143 ensure a proper sealing and airtight conditions of the assembly. In addition, the outer part of the straight
144 union was machined at its center, where the active cell is located, to reduce the wall thickness leading
145 to an outer diameter of about 8 mm thus facilitating X-ray transmission. Despite the better corrosion
146 resistance of stainless-steel, Al current collectors were selected because of its neutron transparency and
147 low radioactive activation under a neutron beam (Girardi and Pietra 1963). To assemble the cell, a first
148 Al piston is inserted followed by the active cell and an Al shim. Then, a stainless-steel spring and a
149 second Al piston conclude the assembly. The spring allows the imposition of a constant load to the
150 active cell while all the Al and stainless-steel parts ensure electronic conduction from the active cell to
151 a potentiostat via conventional ‘crocodile’ clips.

152 The active cell consists in Li symmetric cell assembled in an argon (Ar) filled glovebox (Campus,
153 Jacomex) with sub-ppm values of oxygen and water. For each cell, one electrode is made of natural Li

154 (92.4 % ^7Li and 7.6 % ^6Li) while the other is in ^6Li (95 atom % chunk in mineral oil, Sigma Aldrich).
155 The deuterated liquid electrolyte is formulated in the Ar glovebox by mixing lithium bis-
156 trifluoromethanesulfonimide (LiTFSI) with deuterated dimethyl carbonate (*d*-DMC, Sigma Aldrich,
157 used as received) to attain a 1 M concentration. First, a layer of ^6Li was cut from a larger piece,
158 manually flattened using a roll, and 3 mm diameter disks were punch out. The average thickness of ^6Li
159 electrode is $145 \pm 10 \mu\text{m}$ based on the series of cell replicates. Similarly, 3 mm diameter disks of
160 natural Li were punched out from a Li foil. The PTFE cell were assembled halfway by inserting a first
161 Al piston (see **Figure S1**). The ^6Li electrode was placed inside the cell followed by a 2 mm long
162 perfluoroalkoxy alkane (PFA) tube with a 1/8 inch ($\sim 3.18 \text{ mm}$) outer and 1/16 inch ($\sim 1.59 \text{ mm}$) inner
163 diameter to confine the liquid electrolyte and separate the two electrodes. The tube is filled with the
164 deuterated liquid electrolyte (1M LiTFSI in *d*-DMC) and the natural Li electrode placed on top of the
165 tube. Then, an Al shim, the spring and a second Al piston is inserted and the cell closed. Four cell
166 replicates were assembled and cycled for the purpose of this study.

167 **2.2. Cell cycling**

168 The cell replicates were taken out of the glove box, placed in an oven (UN30, Memmert) held at
169 $25 \text{ }^\circ\text{C}$, and connected to a single-channel potentiostat (SP200, BioLogic) with impedance capability.
170 Then, a constant current of $8.4 \mu\text{A}$ was applied to each cell up to 72.5 h in one direction. During the
171 galvanostatic step, the ^6Li is stripped and plated onto the opposite natural Li electrode. The cell
172 impedances were recorded before and after the galvanostatic step via potentiostatic electrochemical
173 impedance spectroscopy. At the open circuit voltage, an excitation signal of 40 mV is applied to the
174 cell in a frequency range in between 7 MHz and 1 Hz. The impedance spectra were fitted using the Zfit
175 module included in the EC-lab software.

176 **2.3. Electrolyte conductivity**

177 The ionic conductivity of the sole deuterated liquid electrolyte (1M LiTFSI/*d*DMC) was
178 determined as a function of temperature. Inside the Ar glovebox, a conductivity cell for microsample
179 (Hach Co.) was inserted into a test tube filled with the electrolyte and hermetically sealed. The cell was
180 taken out of the glove box and placed in an oven (VTM 4004, Vötsch) to perform impedance
181 measurements at temperature ranging from 25 to $60 \text{ }^\circ\text{C}$ in steps of $10 \text{ }^\circ\text{C}$, then cooled down to $-25 \text{ }^\circ\text{C}$
182 before a final heating scan up to $60 \text{ }^\circ\text{C}$ in steps of $5 \text{ }^\circ\text{C}$. The impedance spectra were fitted using a
183 similar electrical equivalent circuit detailed in a previous report(Devaux et al. 2012) to extract the
184 electrolyte resistance (R_{el}). In addition, the electrode cell constant (k) was determined beforehand via
185 a 0.01 M KCl aqueous solution.

186 **2.4. Neutron tomography**

187 Neutron tomography was performed at the NeXT beamline at the Institut Laue-Langevin (ILL,
188 Grenoble, France) (Tengattini et al. 2020). The cells were mounted on a rotation platform and imaged
189 at room temperature. There, cold neutrons reach the cell after going through a 15 mm diameter pinhole
190 collimator (D), placed at 10 m from the sample (L) without any filter. Given this collimation ratio L/D
191 = 667 and an effective 12 mm cell diameter placed close to the detector, the neutron penumbra

192 (blurring) is estimated to be around 10 μm , close to the pixel size. To detect neutrons a typical
193 scintillator-mirror-camera as well as an infinity-corrected optical system are employed (Tengattini et
194 al. 2020). The Hamamastu Orca Flash 4V2 equipped with Canon 100 mm f./2.0 optics with a 50 μm
195 thick LiF ($^6\text{LiF}/\text{ZnS}:\text{Cu}$) scintillator was firstly employed to gather rough estimates of the geometry of
196 the different cells over a large field of view set at 40 x 40 mm leading to a 20 μm spatial resolution.
197 Once a cell was selected, a second, infinity corrected setup, composed of a 5 μm Gadolinium
198 ($\text{Gd}_2\text{O}_3\text{S}:\text{Tb}/^6\text{LiF}$) scintillator and a combination of a 50 mm f./1.2 Canon lens and a 55 mm Heliflex
199 lens was employed to achieve a 7.4 μm pixel size over a 14 mm field of view. A series of 2600
200 projections, each 25 seconds long were acquired over a 360° rotation, leading to a total acquisition time
201 of 18 h. In the 32 bits reconstructed images via the RX Solutions software which employs a Feldkamp
202 (FDK) filtered back projection algorithm, the grayscale value represents the attenuation coefficient, so
203 more attenuating regions are brighter. The volume obtained was 2575 x 2538 x 3397 μm^3 . Further
204 image analysis was performed using the Fiji software (Schindelin et al. 2012).

205 **2.5. Synchrotron X-ray tomography**

206 Synchrotron X-ray computed tomography (XRCT) using phase contrast was performed at the
207 PSICHE beamline at the Soleil Synchrotron (Gif-sur-Yvette, France) (King et al. 2016). At the
208 beamline, the cell was mounted on a rotating plate and illuminated at room temperature with a pink X-
209 ray beam set at an average energy of 25 keV. A series of 1500 projections along a 180° rotation with
210 an exposure time of 40 ms per projection was acquired. The field of view was restricted to 1.3 x 1.3
211 mm with a 0.64 μm voxel size. The collected radiographs were reconstructed using the PyHST2
212 software (Mirone et al. 2014). Given that the Li cell height comprising the 2 mm long PFA tube is
213 larger than the field of view, two tomographic acquisitions were performed on the cell; one focusing
214 on the top of the active cell to image the natural Li electrode and another one focusing on the lower
215 half of the active cell to image the ^6Li electrode. Each image stack reconstructed in 32 bits floating-
216 point were subsequently merged into a single one. The volume obtained 2510 x 1313 x 1313 μm^3 . The
217 analysis of the images was also performed with the Fiji software.

218 **2.6. Laboratory X-ray tomography**

219 A laboratory X-ray tomograph (EasyTom, RX Solutions) with a LaB_6 cathode source and a
220 Paxscan 2520DX (Varex Imaging) amorphous silicon flat panel detector located at MATEIS laboratory
221 (Villeurbanne, France) was employed to image the cells at room temperature. The detector has 1920
222 rows and 1536 columns of square pixels (each 127 x 127 μm^2 in size) with a CsI scintillator and
223 provides the value of the attenuation with a 16 bits gray level. Each cell was fixed to the scanner
224 rotation platform and a tension of 50 kV was used to acquire the scan. The tomography was acquired
225 over four 360° rotations plus references (for alignment in case of thermo-mechanical misalignments
226 along the test) comprising 1184 images. Each projection was the result of the average of 3 frames at
227 0.70 frames per second, optimized to ensure sufficient X-ray flux to have good signal to noise ratio.
228 The volume obtained was 3422 x 3422 x 2614 μm^3 with an isotropic voxel size of 2 μm . The collected
229 radiographs were reconstructed to produce a 3-dimensional (3D) stack via the RX Solutions software
230 without correction of beam hardening and Fiji software was used for image analysis.

231 3 Results and Discussion

232 To validate the design of the electrochemical cell, a series of uncycled electrochemical cells was
 233 imaged by X-ray tomography at the laboratory source to get insight on the quality of the active cell
 234 assembly (^6Li /electrolyte/Li). **Figure 1** shows a tomography of a cell cross-section acquired at room
 235 temperature. In this figure, the grayscale value for each pixel is the attenuation coefficient of the
 236 corresponding portion of space. So, for example, heavy elements such as Al that strongly absorbs X-
 237 rays appear brighter. The cell casing made of PTFE is transparent enough to the X-ray so that the active
 238 cell and the Al parts (piston or shim) can be distinguished. Due to the slightly higher absorption of
 239 PFA compared to Li and to the polychromatic nature of the laboratory X-ray source, reconstruction
 240 artefacts likely due to the cone beam or beam hardening (Maire and Withers 2014) are observed.
 241 Indeed, the upper Li electrode seems to exhibit two different attenuation values, *i.e.* the pixels
 242 corresponding to the Li electrodes close to the Al materials appear more attenuating than they should
 243 be. In addition, the natural Li electrode located on top of **Figure 1** has similar gray values than the
 244 bottom one made of ^6Li . As expected, X-ray imaging is not sensitive to the Li isotopes making it
 245 impossible to distinguish between these two electrodes (^6Li vs. natural Li). It can also be noticed the
 246 presence of two domains located within the PFA tube, one with grey values close to those of the PFA,
 247 and ascribed to the liquid electrolyte, while the other one presents grey values similar to those of the
 248 Li electrodes suggesting the presence of an Ar bubble. This is explained by the delicate cell assembly
 249 that may entrapped Ar bubble in the liquid electrolyte. Despite the presence of a bubble in **Figure 1**,
 250 the Li electrodes are not perfectly flat as the surface of both Li electrodes facing the liquid electrolyte
 251 tends to adopt a spherical cap shape. This feature observed on all cell replicates is probably due to the
 252 softness of Li compressed within the PFA tube due to the spring pressure and to a mediocre adhesion
 253 of Li with the Al parts. The study of the uncycled cells by X-ray tomography highlights the importance
 254 of the 3D nature of these analyses, as the inner cell geometry must be accounted for electrochemical
 255 and impedance studies. Indeed, the dome surfaces lead to an effective surface and an effective cell
 256 constant that will differ from the geometrical ones. We can consider that the two electrodes formed
 257 equivalent spherical cap spheres within the PFA tube having a radius (r) equivalent to the PFA inner
 258 tube radius, a height (h), and separated by a distance (l) equivalent to the PFA tube height. In such
 259 configuration, the effective cell constant (k) is estimated using the equipotential current line (Hong,
 260 Chong, and Cho 2019) between two domes given by:

$$k = \int_h^{l-h} \frac{1}{\pi \cdot r} \cdot \frac{dx}{x} = \frac{1}{\pi \cdot r} \cdot \ln\left(\frac{l}{h} - 1\right) \quad (1)$$

261 By measuring the distance r , h , and l by laboratory X-ray tomography imaging on a series of four
 262 uncycled cell replicates, the average effective cell constant k is 6.9 ± 0.1 . Impedance spectroscopy was
 263 then performed on the uncycled cell replicates at 25 °C. Considering the effective surface, **Figures 2a**
 264 and **2b** show the impedance spectra in Nyquist coordinates along with the characteristic frequencies of
 265 two typical cells, denoted cell_A and cell_B, respectively. Each spectrum presents two semi-circle
 266 loops, one in the high frequency range between 7 MHz and 100 kHz and another one at lower
 267 frequencies. The high and low frequency loops are ascribed to the electrolyte (R_{el}) and Li/electrolyte

268 interface resistances, respectively (Bouchet, Lascaud, and Rosso 2003). The spectra were fitted with
 269 an electrical equivalent circuit composed of elements in series corresponding to the cable resistance
 270 and inductance, the electrolyte response as R_{el} in parallel with a constant phase element followed by
 271 another resistance in parallel with a constant phase element corresponding to the Li/electrolyte
 272 interfaces. The equivalent circuit is displayed in the inset of **Figure 2a**. The electrolyte and interface
 273 resistances of cell_A are higher than that of cell_B by a factor of 7 and 2, respectively. These higher
 274 resistances are ascribed to the presence of an Ar bubble entrapped within the PFA tube due to a contact
 275 surface reduction which also induces a frequency dispersion as the bubble possesses different
 276 dielectrical properties. Regarding the electrolyte resistance of cell_B, the ionic conductivity (σ) at given
 277 temperature (T) is calculated using the following equation:

$$\sigma(T) = \frac{k}{R_{el}(T)} \quad (2)$$

279 By combining equation (1) and (2), the ionic conductivity of cell_B at 25 °C is $6.6 \cdot 10^{-3} \text{ S.cm}^{-1}$.
 280 For comparison, the conductivity of the sole deuterated liquid electrolyte (1M LiTFSI/dDMC) was
 281 determined using the conductivity cell for microsample (see electrolyte conductivity in the
 282 experimental section). **Figure S2** shows σ of the deuterated electrolyte as a function of the inverse of
 283 the temperature in between -25 and 60 °C. In the temperature range explored, the conductivity presents
 284 two different domains with a transition at about -5 °C corresponding to the electrolyte crystallization.
 285 At 25 °C, the conductivity is $6.6 \pm 0.2 \cdot 10^{-3} \text{ S.cm}^{-1}$. This value is consistent with the one reported by
 286 Dahbi *et al.* of about $7.0 \cdot 10^{-3} \text{ S.cm}^{-1}$ for a non-deuterated 1M LiTFSI/DMC electrolyte at 24.8 °C
 287 (Dahbi *et al.* 2011). Therefore, the conductivity at 25 °C of cell_B lies within the error bar of the value
 288 measured by the conductivity cell. Consequently, the analysis of the electrolyte conductivity of
 289 uncycled ${}^6\text{Li}$ -Li cell by impedance spectroscopy in combination with X-ray tomography validates the
 290 design of electrochemical cell and allow the identification of assembly defects (deformed electrodes
 291 and entrapped gas bubble) that should be taken into account for a future cell assembly optimization.

292 The cell replicates were then cycled at a constant low current of 8.4 μA in order to move ${}^6\text{Li}$
 293 (anode) onto the natural Li electrode (cathode). Considering the effective surface, cell_B was cycled
 294 at 0.53 mA.cm^{-2} . For cell_A, the bubble within the liquid electrolyte induces complex current lines
 295 between the two electrodes, and thus an uncertain current density value. The result of the galvanostatic
 296 step performed on cell_A and cell_B is provided in **Figure 3** showing the cell voltage (E in V vs. Li^+/Li)
 297 as a function of time (t). The voltage profile of cell_B is almost constant at 0.1 V vs. Li^+/Li for 16 h
 298 then increases until a plateau at about 0.45 V vs. Li^+/Li . For cell_A, the voltage profile presents first a
 299 sharp increase after 5 h with a peak at about 1.7 V vs. Li^+/Li at $t = 15$ h, before decreasing to 0.2 V vs.
 300 Li^+/Li at $t = 27.5$ h. For $t > 27.5$ h, the cell voltage becomes similar to that of cell_B with E being
 301 constant at 0.2 V vs. Li^+/Li followed by a slight increase up to a final value of about 0.53 V vs. Li^+/Li ,
 302 in the same range than the one reached by cell_B. The voltage fluctuation and high polarization of
 303 cell_A during the first 27.5 h is attributed to the presence and the movement of the Ar bubble within
 304 the PFA tube during the electrochemical step leading to a geometrical factor modification coupled with
 305 an increase of the Li/electrolyte interface due to heterogeneous electrodeposits (K. N. Wood *et al.*
 306 2016).

307 A similar cell voltage behavior than the one observed for cell_B was reported in the works of
 308 Brissot *et al.* (Brissot et al. 1999b) and Rosso *et al.* (M. Rosso et al. 2001) focusing on the study of Li
 309 dendrite growth mechanisms in Li symmetric cells comprising a polymer electrolyte. The authors show
 310 that below a critical current density (J^*) the ionic concentration profile, and thus the concentration
 311 gradient, throughout the cell evolves to a steady state. The cell voltage attains a constant value which
 312 eventually drops to zero when a dendrite makes a contact between the two electrodes. For $J < J^*$, the
 313 morphology of the electrodeposits observed by Brissot and coworkers (Brissot et al. 1999c) is tortuous,
 314 forming mostly mossy Li with the presence of needle-like dendrites. This behavior was partly
 315 confirmed by Bai *et al.* on Li symmetric cell comprising a liquid electrolyte with an electrode inter-
 316 distance in the range of several millimeters where the electrodeposited Li morphology remains mostly
 317 mossy if the current density is below J^* (Bai et al. 2016). Based on the work of Brissot and coworkers
 318 (Brissot et al. 1999c), J^* is defined as:

$$J^* = \frac{2 \cdot F \cdot C \cdot D}{(1 - t^+) \cdot l} \quad (3)$$

319 with F the Faraday constant, C the concentration of salt in the electrolyte, D the ambipolar diffusion
 320 coefficient, and t^+ the cationic transference number.
 321
 322

323 By considering that the ionic transport properties of the deuterated liquid electrolyte are similar
 324 to that of its non-deuterated counterpart, we can take C , t^+ , and D values equal to 1000 mol.m^{-3} , 0.46,
 325 and $3.46 \cdot 10^{-6} \text{ cm}^2.\text{s}^{-1}$, respectively (Borodin and Smith 2006). Using equation 3 and considering a
 326 distance l equal to the typical PFA tube length of 2 mm, then J^* is 5.8 mA.cm^{-2} . Consequently, the
 327 imposed current density of cell_B corresponds to 9 % of J^* and the voltage behavior falls within the J
 328 $< J^*$ case. For cell_A, despite of the effect of the Ar bubble, its cell voltage profile corresponds also to
 329 the $J < J^*$ case. Indeed, even by considering an active surface being a minor fraction of the effective
 330 surface, the current density remains below the J^* value. Moreover, for cell_B, the total amount of
 331 charges passed during the 54.7 h of the galvanostatic step corresponds to a theoretical displacement of
 332 $139 \text{ }\mu\text{m}$ of ${}^6\text{Li}$ based on the Faraday law and considering the effective surface. This value is close to
 333 the ${}^6\text{Li}$ electrode thickness used in cell_B of $145 \text{ }\mu\text{m}$ which means that a quasi-total ${}^6\text{Li}$ oxidation was
 334 performed during current imposition. Therefore, for both cells their current densities used for the Li
 335 transfer from the anode to the cathode lies in the $J < J^*$ case and the length of the PFA tube permit to
 336 oxidize most of the anode (${}^6\text{Li}$) onto the cathode (natural Li) without dendrite short-circuit.
 337

338 At the end of the galvanostatic step, a final impedance measurement was performed on cell_A
 339 and cell_B, and the corresponding spectra are added in **Figure 2a** and **2b**, respectively. For cell_A, the
 340 total cell resistance is diminished by a factor 3 compared to its initial state with a strong reduction of
 341 the interface resistance by a factor 18 in the lower frequencies range. This situation is certainly due to
 342 an increase in the active surface on the cathode by the growth of mossy or dendritic electrodeposits (as
 343 shown later by Neutron imaging in **Figure 4**) as well as a modification of the solid electrolyte
 344 interphase (X. B. Cheng et al. 2016) on the anode (M. Rosso et al. 2006). In addition, the electrolyte
 345 loop is depressed with a resistance value similar to the initial one which is ascribed to the presence of

346 both Li deposits and bubble within the liquid electrolyte inducing a strong dispersion in the
347 characteristic frequencies. For cell_B, the total cell resistance increased by a factor 1.4 with the main
348 change observed for the electrolyte resistance (high frequency loop) while the characteristic
349 frequencies of the two loops are modified. This behavior may be due to a cell constant modification
350 during the galvanostatic step. Based on **Figure 1**, the ${}^6\text{Li}$ takes the form of a dome on top of the Al
351 current collector, so the cell constant will gradually change towards a higher constant value while the
352 anode (${}^6\text{Li}$) is oxidized, and conversely, electrodeposits formed onto the cathode, until most of the ${}^6\text{Li}$
353 is consumed inducing a hole in the anode.

354

355 After the galvanostatic step, the electrochemical cells were taken to the neutron tomography
356 beamline for an *in situ* imaging at room temperature. There, a series of radiographies was first acquired
357 at a large field of view and at different rotation angles in order to quickly inspect each cell. Except
358 cell_A, the radiographies of cell_B and other replicates revealed a damaged assembly and thus were
359 discarded for further tomography imaging. For cell_A, a typical radiography is reported in **Figure 4a**
360 where at each pixel, the gray value is proportional to the neutron attenuation of the corresponding
361 region of space. In this image, neutron transparent materials such as Al (piston and shim) and PTFE
362 (cell casing) appear brighter (given that most of the neutrons are transmitted to the detector) than
363 material with stronger neutron attenuation such as the stainless steel spring or Li electrodes (Sears
364 1992). As expected, the Al and PFA materials are suitable for neutron imaging as their attenuation is
365 essentially negligible. The top and bottom Li electrodes appear black in between the Al parts and PFA
366 tube. In addition, the PFA inner surface is visible from the overall background because of the presence
367 of absorbent materials within the deuterated electrolyte, with from top to bottom as detailed in **Figure**
368 **4a**: the natural Li electrode (the cathode in the galvanostatic step) with a spherical cap shape as
369 observed in the uncycled cell through X-ray tomography (see **Figure 1**), the ${}^6\text{Li}$ deposits in the
370 electrolyte, and a less attenuating portion at the bottom suggesting the presence of a bubble. It can be
371 noted that at the bottom of the PFA tube, the ${}^6\text{Li}$ electrode is almost absent from the radiography in
372 agreement with its quasi-total oxidation during the electrochemical step (see **Figure 3**). Moreover, at
373 the interface between the PFA tube and the Al parts on both side of the cell, a highly attenuating
374 material is covering the Al surface as well as on its edges. This is attributed to a chemical and
375 electrochemical degradation of Al areas in contact with Li metal. Tahmasebi *et al.* recently reported
376 on the degradation of Al surface associated with the formation of the LiAl (β) phase either during
377 electrochemical lithiation or by simple contact between Al and Li metal (Tahmasebi et al. 2019).
378 Cell_A was subsequently imaged in tomography for 18 hours. **Figure 4b** shows a typical vertical slice
379 of the tomography, showing a cross-section of cell_A. The values of the voxels in a tomography are
380 related to the attenuation coefficients of the corresponding volume of space with higher values for
381 highly attenuating materials which is the opposite to the radiography images. As observed in the
382 radiography, both Al parts in contact with Li are highly attenuating, indicating the presence of the LiAl
383 phase. At the bottom part, the few ${}^6\text{Li}$ anode remainders appear in bright white. The gray values of the
384 ${}^6\text{Li}$ throughout the reconstructed volume are the highest of all observed materials in the active cell with
385 some gray saturation at some voxels as shown in the bottom right corner. As expected, the gray values
386 associated to the natural Li electrode (the bended electrode at the top of **Figure 4b**) are lower than that
387 of the ${}^6\text{Li}$, as its theoretical neutron attenuation coefficient is 15 times lower (Sears 1992). This result

388 shows that the Li isotope sensibility to neutron is an effective tool to differentiate between Li electrodes
389 (^6Li vs. natural Li) after an electrochemical step. Moreover, inside the electrolyte volume in **Figure**
390 **4b**, a highly neutron attenuating, irregularly shaped domain is observed and attributed to ^6Li deposits,
391 appearing in light-gray and white, originating from the natural Li electrode and spreading throughout
392 the electrolyte. In this experiment, the attenuation values from the ^6Li deposits are in the same range
393 as that of the natural Li electrode and of the Li reacted with Al leading to difficulties in distinguishing
394 between each of these domains. Indeed, even if the voxel size is larger than the characteristic diameter
395 of mossy Li or Li dendrites (Bai et al. 2016), the ^6Li deposits are visible because of the partial volume
396 effect (Santago and Gage 1995; Kaestner et al. 2013). Typically, the attenuation coefficient of voxels
397 partially occupied by both deposits and electrolyte will be intermediate between the attenuation of the
398 individual components. The ^6Li deposits are also surrounding a dark-gray black volume with gray
399 values close to that of the background air, and having a bulb shape confirming to the presence of a
400 bubble.

401

402 From the tomography imaging, the active cell volume can be segmented in different components,
403 based on their gray level. The Al domain can be easily segmented as it has significantly lower
404 attenuation values. The segmentation of the other domains containing Li (deposits, cathode and the
405 LiAl alloy) is more delicate, given the comparable attenuation values. The thresholding limits between
406 these is therefore more arbitrary. **Figure 4c** corresponds to the segmentation of the slice shown in
407 **Figure 4b** while a 3D volume rendering is shown in **Figure 4d**. The ^6Li deposits within the electrolyte
408 take the form of a heterogeneous ramified structure. Beside this graphical representation, the
409 segmentation allows a quantitative analysis. The overall deposits volume can be calculated by summing
410 all the voxels attributed to this material. The result of $0.48 \pm 0.10 \text{ mm}^3$ is given in **Table 1**. This value
411 is overestimated as the image resolution is larger than typical electrodeposits dimensions (Bai et al.
412 2016). It follows that, depending on the threshold value chosen for the segmentation, an overestimation
413 of the deposit volume is probable which tends to increase with the amount of porosity. So, even if the
414 microstructure has typical dimensions smaller than that of the tomography resolution, this proof-of-
415 concept experiment highlights the potential of neutron imaging in determining the overall shape and
416 nature of heterogeneous electrodeposits as well as cell assembly defects within electrochemical cell
417 comprising X-ray attenuating materials.

418

419 To get further insight on the fine structure of the deposits, cell_A was then imaged at a
420 synchrotron X-ray tomography beamline. A typical tomography image of the entire cross-section of
421 the active cell is shown in **Figure 5a**. Thanks to the voxel size of $0.64 \mu\text{m}$, the ^6Li deposits are clearly
422 seen as they attenuate less X-rays than the liquid electrolyte. The ^6Li deposits develop a needle-like
423 dendritic morphology in accordance with the finding of Brissot and coworker (Brissot et al. 1999c). In
424 addition, the LiAl domain is easily discernable at the top and bottom part of the cell showing interface
425 degradation. A segmentation process was then performed on the X-ray images and the dendrites in the
426 electrolyte were segmented based on their gray level (very dark dendrites). However, synchrotron
427 tomography has a very coherent X-ray source leading to dark/light fringes due to phase contrast
428 (Vanpeene et al. 2020). As seen in **Figure 5a**, the interfaces of the curved Li foil have different gray
429 levels. An automatic grayscale segmentation of the curved foil was therefore unsatisfactory and thus

430 manually corrected. An illustration of this process is provided in **Figure 5b** and the resulting 3D
431 rendering volume in **Figure 5c**. From this segmentation process, the dendrite volume was calculated
432 to be $0.14 \pm 0.01 \text{ mm}^3$, a value also included in **Table 1**. A factor of 3.4 separates the dendrite volume
433 measured by neutron and synchrotron X-ray analysis which is mainly due to the difference in imaging
434 resolution.

435 For completeness, cell_A was imaged at the laboratory X-ray tomograph with a $2.0 \mu\text{m}$ voxel
436 size. In **Figure 6a**, a cross-section image corresponding to the same area as the one reported in **Figure**
437 **5a** is shown. Similar observations of the cell can be made compared to the synchrotron X-ray and
438 neutron based images. It should also be noted that the cell was imaged at the neutron and X-ray
439 beamlines, and laboratory tomograph within few weeks. The morphology of the electrodeposit is then
440 preserved over time. Therefore, post-cycling analyses can be performed with confidence several days
441 or weeks after the electrochemical experiment. After the scan, the segmentation process was performed
442 and the dendrite volume was reconstructed in 3D as depicted in **Figure 6b** and **6c**, respectively. A Li
443 dendrite volume of $0.15 \pm 0.02 \text{ mm}^3$ was calculated, a value also reported in **Table 1** which is in the
444 same range than the one obtained from synchrotron X-ray imaging. This result is in agreement with
445 the fact that the signal-to-noise and contrast-to-noise ratios of a laboratory tomograph is lower than for
446 synchrotron beamlines leading to lower resolution images with lower contrasts (Vanpeene et al.
447 2020b). The dendrite volumes measured with the X-ray sources are similar while at larger voxel size
448 by neutron tomography the measured dendrite volume is higher by at least a factor 3 with higher
449 uncertainty. This difference is attributed to lower resolution of the neutron tomography images leading
450 to the selection of voxels comprising a mixture of Li dendrite and electrolyte (partial volume effect)
451 during the segmentation process. While the neutron imaging resolution is unavoidably lower because
452 of the technical constraints of the technique, the capacity of neutrons to discern different isotopes can
453 be exploited to pinpoint the origin and the composition of the Li comprising the dendrites. It would
454 then be of interest to discern the chemical composition within dendrites between Li originating from
455 the anode (^6Li in this study) to that from the Li salt of the electrolyte (mainly in ^7Li here).

456

457 **4 Conclusion**

458 We report an *in situ* neutron tomography imaging of Li electrodeposits in a cycled ^6Li -Li cell by
459 taking advantage of the capability of the neutron imaging beamline and the intrinsic contrast of Li
460 isotopes to neutron. This proof-of-concept experiment shows that the overall morphology of the
461 deposits can be captured by neutron tomography. The deposit volume could be measured and compared
462 to those obtained by X-ray techniques. To go further, several experimental parameters need to be
463 optimized to move towards higher resolution and contrast in shorter acquisition times. For the proposed
464 electrochemical cell, the use of neutron transparent buffer metal layer in between Al parts and Li metal
465 while being chemically and electrochemically stable is a necessity as is the reduction of the cell
466 diameter. As for the beamline, the foreseen increase in capabilities will permit to close the resolution
467 and contrast gap between neutron and laboratory X-ray tomograph. In addition, the study of uncycled
468 cell also highlights the importance of 3D analyses in order to validate the design of electrochemical
469 cell as it allows the identification of assembly defects such as deformed electrodes or entrapped gas
470 bubble that must be taken into account for electrochemical and impedance measurements. *In situ*

471 neutron tomography permits to envision the thorough study of battery failure modes in electrochemical
472 cells comprising X-ray attenuating materials. The capacity of neutrons to discern different isotopes can
473 be then a tool get insight on the origin and the composition of the Li deposits by distinguishing between
474 Li from the anode (${}^6\text{Li}$ is this study) to that from the Li salt electrolyte (mainly in ${}^7\text{Li}$ here).

475

476 **5 Conflict of Interest**

477 The authors declare that the research was conducted in the absence of any commercial or
478 financial relationships that could be construed as a potential conflict of interest.

479 **6 Author Contributions**

480 DD, AT, FA, RB, and LL designed the project study. LM, LL, EM, AK, RB, AT, and DD
481 conducted the experiments. LM, LL, EM, RB, AT, and DD analyzed the data. LM, FA, EM, RB, AT,
482 and DD wrote the manuscript. All the authors commented on the manuscript.

483 **7 Funding**

484 This work was supported by the French Agence Nationale de la Recherche ANR grant
485 SHUTTLE (ANR-19-CE05-0023).

486 **8 Acknowledgments**

487 We acknowledge the French Agence Nationale de la Recherche ANR for its financial support. A
488 portion of this work was performed through beamtime proposal to the NeXT beamline at ILL
489 (beamtime no. UGA-52 and UGA-91) and PSICHE beamline at the SOLEIL synchrotron (beamtime
490 no. 20190532)

491 **9 References**

492 Aurbach, D., E. Zinigrad, H. Teller, and P. Dan. 2000. "Factors Which Limit the Cycle Life of
493 Rechargeable Lithium (Metal) Batteries." *Journal of The Electrochemical Society* 147: 1274.
494 <https://doi.org/10.1149/1.1393349>.

495 Bai, Peng, Ju Li, Fikile R. Brushett, and Martin Z. Bazant. 2016. "Transition of Lithium Growth
496 Mechanisms in Liquid Electrolytes." *Energy and Environmental Science* 9: 3221–29.
497 <https://doi.org/10.1039/c6ee01674j>.

498 Banhart, John, András Borbély, Krzysztof Dzieciol, Francisco Garcia-Moreno, Ingo Manke, Nikolay
499 Kardjilov, Anke Rita Kaysser-Pyzalla, Markus Strobl, and Wolfgang Treimer. 2010. "X-Ray
500 and Neutron Imaging - Complementary Techniques for Materials Science and Engineering."
501 *International Journal of Materials Research* 101: 1069–79. <https://doi.org/10.3139/146.110382>.

502 Borodin, Oleg, and Grant D. Smith. 2006. "Development of Many-Body Polarizable Force Fields for
503 Li-Battery Applications: 2. LiTFSI-Doped Oligoether, Polyether, and Carbonate-Based

- 504 Electrolytes.” *Journal of Physical Chemistry B* 110: 6293–99.
505 <https://doi.org/10.1021/jp055080d>.
- 506 Bouchet, R, S Lascaud, and M Rosso. 2003. “An EIS Study of the Anode Li/PEO-LiTFSI of a Li
507 Polymer Battery.” *Journal of the Electrochemical Society* 150: A1385–89.
508 <https://doi.org/10.1149/1.1609997>.
- 509 Brissot, C, M Rosso, J.-N. Chazalviel, and S Lascaud. 1999a. “In Situ Concentration Cartography in
510 the Neighborhood of Dendrites Growing in Lithium/Polymer-Electrolyte/Lithium Cells.”
511 *Journal of the Electrochemical Society* 146: 4393–4400. <https://doi.org/10.1149/1.1392649>.
- 512 Brissot, C., M. Rosso, J.-N. Chazalviel, and S. Lascaud. 1999b. “Dendritic Growth Mechanisms in
513 Lithium/Polymer Cells.” *Journal of Power Sources* 81–82: 925–29.
514 [https://doi.org/10.1016/S0378-7753\(98\)00242-0](https://doi.org/10.1016/S0378-7753(98)00242-0).
- 515 Bruce, P G, S A Freunberger, L J Hardwick, and J.-M. Tarascon. 2012. “Li–O₂ and Li–S Batteries
516 with High Energy Storage.” *Nature Materials* 11: 19–29. <https://doi.org/10.1038/nmat3191>.
- 517 Butler, Leslie G., Burkhard Schillinger, Kyungmin Ham, Tabbetha A. Dobbins, Ping Liu, and John J.
518 Vajo. 2011. “Neutron Imaging of a Commercial Li-Ion Battery during Discharge: Application of
519 Monochromatic Imaging and Polychromatic Dynamic Tomography.” *Nuclear Instruments and
520 Methods in Physics Research, Section A: Accelerators, Spectrometers, Detectors and Associated
521 Equipment* 651: 320–28. <https://doi.org/10.1016/j.nima.2011.03.023>.
- 522 Cheng, Xin Bing, Rui Zhang, Chen Zi Zhao, Fei Wei, Ji Guang Zhang, and Qiang Zhang. 2016. “A
523 Review of Solid Electrolyte Interphases on Lithium Metal Anode.” *Advanced Science* 3:
524 1500213. <https://doi.org/10.1002/advs.201500213>.
- 525 Cheng, Xin-Bing, Rui Zhang, Chen-Zi Zhao, and Qiang Zhang. 2017. “Toward Safe Lithium Metal
526 Anode in Rechargeable Batteries: A Review.” *Chemical Reviews* 117: 10403–73.
527 <https://doi.org/10.1021/acs.chemrev.7b00115>.
- 528 Dahbi, Mouad, Fouad Ghamouss, François Tran-Van, Daniel Lemordant, and Mérièm Anouti. 2011.
529 “Comparative Study of EC/DMC LiTFSI and LiPF₆ Electrolytes for Electrochemical Storage.”
530 *Journal of Power Sources* 196: 9743–50. <https://doi.org/10.1016/j.jpowsour.2011.07.071>.
- 531 Devaux, D., R. Bouchet, D. Glé, and R. Denoyel. 2012. “Mechanism of Ion Transport in
532 PEO/LiTFSI Complexes: Effect of Temperature, Molecular Weight and End Groups.” *Solid
533 State Ionics* 227: 119–217. <https://doi.org/10.1016/j.ssi.2012.09.020>.
- 534 Devaux, D., K.J. Harry, D.Y. Parkinson, R. Yuan, D.T. Hallinan, A.A. MacDowell, and N.P. Balsara.
535 2015. “Failure Mode of Lithium Metal Batteries with a Block Copolymer Electrolyte Analyzed
536 by X-Ray Microtomography.” *Journal of the Electrochemical Society* 162: A1301–A1309
537 <https://doi.org/10.1149/2.0721507jes>.
- 538 Foroozan, Tara, Soroosh Sharifi-Asl, and Reza Shahbazian-Yassar. 2020. “Mechanistic
539 Understanding of Li Dendrites Growth by In- Situ/Operando Imaging Techniques.” *Journal of
540 Power Sources* 461: 228135. <https://doi.org/10.1016/j.jpowsour.2020.228135>.

- 541 Girardi, Francesco., and Romano. Pietra. 1963. "Neutron Activation Analysis of Aluminum.
542 Determination of Gamma-Emitting Impurities with Long Half Lives." *Analytical Chemistry* 35:
543 173–77. <https://doi.org/10.1021/ac60195a020>.
- 544 Gireaud, L, S Grugeon, S Laruelle, B Yrieix, and J.-M. Tarascon. 2006. "Lithium Metal
545 Stripping/Plating Mechanisms Studies: A Metallurgical Approach." *Electrochemistry*
546 *Communications* 8: 1639–49. <https://doi.org/10.1016/j.elecom.2006.07.037>.
- 547 Grey, C. P., and J. M. Tarascon. 2017. "Sustainability and in Situ Monitoring in Battery
548 Development." *Nature Materials* 16: 45–56. <https://doi.org/10.1038/nmat4777>.
- 549 Harry, Katherine J, Daniel T Hallinan, Dilworth Y Parkinson, Alastair A MacDowell, and Nitash P
550 Balsara. 2014. "Detection of Subsurface Structures Underneath Dendrites Formed on Cycled
551 Lithium Metal Electrodes." *Nature Materials* 13: 69–73. <https://doi.org/10.1038/nmat3793>.
- 552 Hong, Chang-Ho, Song-Hun Chong, and Gye-Chun Cho. 2019. "Theoretical Study on Geometries of
553 Electrodes in Laboratory Electrical Resistivity Measurement." *Applied Sciences (Switzerland)* 9:
554 4167. <https://doi.org/10.3390/app9194167>.
- 555 Ilott, Andrew J., Mohaddese Mohammadi, Hee Jung Chang, Clare P. Grey, and Alexej Jerschow.
556 2016. "Real-Time 3D Imaging of Microstructure Growth in Battery Cells Using Indirect MRI."
557 *Proceedings of the National Academy of Sciences of the United States of America* 113: 10779–
558 84. <https://doi.org/10.1073/pnas.1607903113>.
- 559 Kaestner, A.P., E. H. Lehmann, J. Hovind, M. J. Radebe, F. C. de Beer, and C.M. Sim. 2013.
560 "Verifying Neutron Tomography Performance Using Test Objects." *Physics Procedia* 43: 128–
561 37. <https://doi.org/10.1016/j.phpro.2013.03.016>.
- 562 King, A., N. Guignot, P. Zerbino, E. Boulard, K. Desjardins, M. Bordessoule, N. Leclercq, et al. 2016.
563 "Tomography and Imaging at the PSICHE Beam Line of the SOLEIL Synchrotron." *Review of*
564 *Scientific Instruments* 87: 093704. <https://doi.org/10.1063/1.4961365>.
- 565 Knoche, Thomas, Veronika Zinth, Michael Schulz, Joscha Schnell, Ralph Gilles, and Gunther
566 Reinhart. 2016. "In Situ Visualization of the Electrolyte Solvent Filling Process by Neutron
567 Radiography." *Journal of Power Sources* 331: 267–76.
568 <https://doi.org/10.1016/j.jpowsour.2016.09.037>.
- 569 Li, Wangda, Bohang Song, and Arumugam Manthiram. 2017. "High-Voltage Positive Electrode
570 Materials for Lithium-Ion Batteries." *Chemical Society Reviews* 46: 3006–59.
571 <https://doi.org/10.1039/c6cs00875e>.
- 572 Li, Zhe, Jun Huang, Bor Yann Liaw, Viktor Metzler, and Jianbo Zhang. 2014. "A Review of Lithium
573 Deposition in Lithium-Ion and Lithium Metal Secondary Batteries." *Journal of Power Sources*
574 254 (May): 168–82. <https://doi.org/10.1016/j.jpowsour.2013.12.099>.
- 575 Magnier, Lucile, Didier Devaux, Joël Lachambre, Margaud Lecuyer, Marc Deschamps, Renaud
576 Bouchet, and Eric Maire. 2020. "Quantification of the Local Topological Variations of Stripped
577 and Plated Lithium Metal by X-Ray Tomography." *ACS Applied Materials & Interfaces* 12:
578 41390–97. <https://doi.org/10.1021/acsami.0c10860>.

- 579 Maire, E., J. Y. Buffière, L. Salvo, J. J. Blandin, W. Ludwig, and J. M. Létang. 2001. “On the
580 Application of X-Ray Microtomography in the Field of Materials Science.” *Advanced*
581 *Engineering Materials* 3: 539–46. [https://doi.org/10.1002/1527-2648\(200108\)3:8<539::AID-
582 ADEM539>3.0.CO;2-6](https://doi.org/10.1002/1527-2648(200108)3:8<539::AID-ADEM539>3.0.CO;2-6).
- 583 Maire, E., and P. J. Withers. 2014. “Quantitative X-Ray Tomography.” *International Materials*
584 *Reviews* 59: 1–43. <https://doi.org/10.1179/1743280413Y.0000000023>.
- 585 Manke, I., J. Banhart, A. Haibel, A. Rack, S. Zabler, N. Kardjilov, A. Hilger, A. Melzer, and H.
586 Riesemeier. 2007. “In Situ Investigation of the Discharge of Alkaline Zn-MnO₂ Batteries with
587 Synchrotron X-Ray and Neutron Tomographies.” *Applied Physics Letters* 90: 214102.
588 <https://doi.org/10.1063/1.2742283>.
- 589 Mirone, Alessandro, Emmanuel Brun, Emmanuelle Gouillart, Paul Tafforeau, and Jerome Kieffer.
590 2014. “The PyHST2 Hybrid Distributed Code for High Speed Tomographic Reconstruction with
591 Iterative Reconstruction and a Priori Knowledge Capabilities.” *Nuclear Instruments and*
592 *Methods in Physics Research Section B: Beam Interactions with Materials and Atoms* 324: 41–
593 48. <https://doi.org/10.1016/j.nimb.2013.09.030>.
- 594 Morigaki, K., and A Ohta. 1998. “Analysis of the Surface of Lithium in Organic Electrolyte by
595 Atomic Force Microscopy, Fourier Transform Infrared Spectroscopy and Scanning Auger
596 Electron Microscopy.” *Journal of Power Sources* 76: 159–66. [https://doi.org/10.1016/S0378-
597 7753\(98\)00151-7](https://doi.org/10.1016/S0378-7753(98)00151-7).
- 598 Nanda, Jagjit, Hassina Bilheux, Sophie Voisin, Gabriel M. Veith, Richard Archibald, Lakeisha
599 Walker, Srikanth Allu, Nancy J. Dudney, and Sreekanth Pannala. 2012. “Anomalous Discharge
600 Product Distribution in Lithium-Air Cathodes.” *Journal of Physical Chemistry C* 116: 8401–8.
601 <https://doi.org/10.1021/jp3016003>.
- 602 Owejan, Jon P., Jeffrey J. Gagliardo, Stephen J. Harris, Howard Wang, Daniel S. Hussey, and David
603 L. Jacobson. 2012. “Direct Measurement of Lithium Transport in Graphite Electrodes Using
604 Neutrons.” *Electrochimica Acta* 66: 94–99. <https://doi.org/10.1016/j.electacta.2012.01.047>.
- 605 Pietsch, Patrick, and Vanessa Wood. 2017. “X-Ray Tomography for Lithium Ion Battery Research:
606 A Practical Guide.” *Annual Review of Materials Research* 47 (July): 451–79.
607 <https://doi.org/10.1146/annurev-matsci-070616-123957>.
- 608 Riley, Grant V., Daniel S. Hussey, and David Jacobson. 2010. “In Situ Neutron Imaging Of Alkaline
609 and Lithium Batteries.” *ECS Transactions* 25: 75–83. <https://doi.org/10.1149/1.3414005>.
- 610 Rosso, M., T. Gobron, C. Brissot, J. N. Chazalviel, and S. Lascaud. 2001. “Onset of Dendritic
611 Growth in Lithium/Polymer Cells.” *Journal of Power Sources* 97–98: 804–6.
612 [https://doi.org/10.1016/S0378-7753\(01\)00734-0](https://doi.org/10.1016/S0378-7753(01)00734-0).
- 613 Rosso, Michel, Claire Brissot, Anna Teyssot, Mickaël Dollé, Lucas Sannier, Jean Marie Tarascon,
614 Renaud Bouchet, and Stéphane Lascaud. 2006. “Dendrite Short-Circuit and Fuse Effect on
615 Li/Polymer/Li Cells.” *Electrochimica Acta* 51: 5334–40.
616 <https://doi.org/10.1016/j.electacta.2006.02.004>.

- 617 Santago, P., and H. D. Gage. 1995. “Statistical Models of Partial Volume Effect.” *IEEE Transactions*
618 *on Image Processing* 4: 1531–40. <https://doi.org/10.1109/83.469934>.
- 619 Schindelin, Johannes, Ignacio Arganda-Carreras, Erwin Frise, Verena Kaynig, Mark Longair, Tobias
620 Pietzsch, Stephan Preibisch, et al. 2012. “Fiji: An Open-Source Platform for Biological-Image
621 Analysis.” *Nature Methods* 9: 676–82. <https://doi.org/10.1038/nmeth.2019>.
- 622 Schröder, D., C. L. Bender, T. Arlt, M. Osenberg, A. Hilger, S. Risse, M. Ballauff, I. Manke, and J.
623 Janek. 2016. “In Operando X-Ray Tomography for next-Generation Batteries: A Systematic
624 Approach to Monitor Reaction Product Distribution and Transport Processes.” *Journal of*
625 *Physics D: Applied Physics* 49: 404001. <https://doi.org/10.1088/0022-3727/49/40/404001>.
- 626 Sears, Varley F. 1992. “Neutron Scattering Lengths and Cross Sections.” *Neutron News* 3: 26–37.
627 <https://doi.org/10.1080/10448639208218770>.
- 628 Senyshyn, A., M. J. Mühlbauer, K. Nikolowski, T. Pirling, and H. Ehrenberg. 2012. “‘In-Operando’
629 Neutron Scattering Studies on Li-Ion Batteries.” *Journal of Power Sources* 203: 126–29.
630 <https://doi.org/10.1016/j.jpowsour.2011.12.007>.
- 631 Song, Bohang, Indu Dhiman, John C. Carothers, Gabriel M. Veith, Jue Liu, Hassina Z. Bilheux, and
632 Ashfia Huq. 2019. “Dynamic Lithium Distribution upon Dendrite Growth and Shorting
633 Revealed by Operando Neutron Imaging.” *ACS Energy Letters* 4: 2402–8.
634 <https://doi.org/10.1021/acsenenergylett.9b01652>.
- 635 Strobl, M., I. Manke, N. Kardjilov, A. Hilger, M. Dawson, and J. Banhart. 2009. “Advances in
636 Neutron Radiography and Tomography.” *Journal of Physics D: Applied Physics* 42: 243001.
637 <https://doi.org/10.1088/0022-3727/42/24/243001>.
- 638 Sun, Fu, Rui Gao, Dong Zhou, Markus Osenberg, Kang Dong, Nikolay Kardjilov, André Hilger, et
639 al. 2019. “Revealing Hidden Facts of Li Anode in Cycled Lithium–Oxygen Batteries through X-
640 Ray and Neutron Tomography.” *ACS Energy Letters* 4: 306–16.
641 <https://doi.org/10.1021/acsenenergylett.8b02242>.
- 642 Sun, Fu, Henning Markötter, Ingo Manke, André Hilger, Saad S. Alrwashdeh, Nikolay Kardjilov,
643 and John Banhart. 2017. “Complementary X-Ray and Neutron Radiography Study of the Initial
644 Lithiation Process in Lithium-Ion Batteries Containing Silicon Electrodes.” *Applied Surface*
645 *Science* 399: 359–66. <https://doi.org/10.1016/j.apsusc.2016.12.093>.
- 646 Sun, Fu, Lukas Zielke, Henning Markötter, André Hilger, Dong Zhou, Riko Moroni, Roland
647 Zengerle, Simon Thiele, John Banhart, and Ingo Manke. 2016. “Morphological Evolution of
648 Electrochemically Plated/Stripped Lithium Microstructures Investigated by Synchrotron X-Ray
649 Phase Contrast Tomography.” *ACS Nano* 10: 7990–97.
650 <https://doi.org/10.1021/acsnano.6b03939>.
- 651 Tahmasebi, Mohammad Hossein, Dominik Kramer, Reiner Mönig, and Steven T. Boles. 2019.
652 “Insights into Phase Transformations and Degradation Mechanisms in Aluminum Anodes for
653 Lithium-Ion Batteries.” *Journal of The Electrochemical Society* 166: A5001–7.
654 <https://doi.org/10.1149/2.0011903jes>.

- 655 Tan, Chun, Sohrab R. Daemi, Oluwadamilola O. Taiwo, Thomas M.M. Heenan, Daniel J.L. Brett,
656 and Paul R. Shearing. 2018. "Evolution of Electrochemical Cell Designs for In-Situ and
657 Operando 3D Characterization." *Materials* 11: 2157. <https://doi.org/10.3390/ma11112157>.
- 658 Tengattini, Alessandro, Nicolas Lenoir, Edward Andò, Benjamin Giroud, Duncan Atkins, Jerome
659 Beaucour, and Gioacchino Viggiani. 2020. "NeXT-Grenoble, the Neutron and X-Ray
660 Tomograph in Grenoble." *Nuclear Instruments and Methods in Physics Research, Section A:
661 Accelerators, Spectrometers, Detectors and Associated Equipment* 968: 163939.
662 <https://doi.org/10.1016/j.nima.2020.163939>.
- 663 Vanpeene, Victor, Julie Villanova, Jussi Petteri Suuronen, Andrew King, Anne Bonnin, Julien
664 Adrien, Eric Maire, and Lionel Roué. 2020. "Monitoring the Morphological Changes of Si-
665 Based Electrodes by X-Ray Computed Tomography: A 4D-Multiscale Approach." *Nano Energy*
666 74: 104848. <https://doi.org/10.1016/j.nanoen.2020.104848>.
- 667 Wang, Howard, R. Gregory Downing, Joseph A. Dura, and Daniel S. Hussey. 2012. "In Situ Neutron
668 Techniques for Studying Lithium Ion Batteries." In *Polymers for Energy Storage and Delivery:
669 Polyelectrolytes for Batteries and Fuel Cells*, ACS Sympos. Vol. 1096, ACS, Washington, DC,
670 91–106. <https://doi.org/10.1021/bk-2012-1096.ch006>.
- 671 Whittingham, M S. 2004. "Lithium Batteries and Cathode Materials." *Chemical Reviews* 104: 4271–
672 4301. <https://doi.org/10.1021/cr020731c>.
- 673 Wood, Kevin N., Eric Kazyak, Alexander F. Chadwick, Kuan Hung Chen, Ji Guang Zhang, Katsuyo
674 Thornton, and Neil P. Dasgupta. 2016. "Dendrites and Pits: Untangling the Complex Behavior
675 of Lithium Metal Anodes through Operando Video Microscopy." *ACS Central Science* 2: 790–
676 801. <https://doi.org/10.1021/acscentsci.6b00260>.
- 677 Wood, Vanessa. 2018. "X-Ray Tomography for Battery Research and Development." *Nature
678 Reviews Materials* 3: 293–95. <https://doi.org/10.1038/s41578-018-0053-4>.
- 679 Zhang, Y., K. S. Ravi Chandran, M. Jagannathan, H. Z. Bilheux, and J. C. Bilheux. 2017. "The
680 Nature of Electrochemical Delithiation of Li-Mg Alloy Electrodes: Neutron Computed
681 Tomography and Analytical Modeling of Li Diffusion and Delithiation Phenomenon." *Journal
682 of The Electrochemical Society* 164: A28–38. <https://doi.org/10.1149/2.0051702jes>.
- 683 Ziesche, Ralf F., Tobias Arlt, Donal P. Finegan, Thomas M.M. Heenan, Alessandro Tengattini,
684 Daniel Baum, Nikolay Kardjilov, et al. 2020. "4D Imaging of Lithium-Batteries Using
685 Correlative Neutron and X-Ray Tomography with a Virtual Unrolling Technique." *Nature
686 Communications* 11. <https://doi.org/10.1038/s41467-019-13943-3>.
- 687 Ziesche, Ralf F., James B. Robinson, Matthew D. R. Kok, Henning Markötter, Winfried
688 Kockelmann, Nikolay Kardjilov, Ingo Manke, Dan J. L. Brett, and Paul R. Shearing. 2020. "
689 Editors' Choice—4D Neutron and X-Ray Tomography Studies of High Energy Density Primary
690 Batteries: Part I. Dynamic Studies of LiSOCl₂ during Discharge ." *Journal of The
691 Electrochemical Society* 167:130545. <https://doi.org/10.1149/1945-7111/abbbbc>.

692

693

694

695 **10 Table**

Tomography	Synchrotron X-ray	X-ray laboratory	Neutron
Voxel size (μm)	0.64	2.0	7.4
^6Li deposit volume (mm^3)	0.14 ± 0.01	0.15 ± 0.02	0.48 ± 0.10

696 **Table 1.** Comparison of the ^6Li deposit volume from the volume segmentation process depending on
 697 the tomography techniques and their voxel size.

698

699 **11 Figure captions**

700 **Figure 1.** X-ray tomography image of an uncycled ^6Li -Li cell using a laboratory scanner and recorded
 701 at room temperature.

702 **Figure 2.** Impedance spectra recorded at 25 °C of the electrochemical cells (filled symbols) before and
 703 (open symbols) after cycling for (A) cell_A and (B) cell_B. The inset in (A) shows the electrical
 704 equivalent circuit used to fit all the spectra.

705 **Figure 3.** Cell voltage at 25 °C during the galvanostatic step for (solid curve) cell_A and (dotted curve)
 706 cell_B.

707 **Figure 4.** Typical image of the cycled ^6Li -Li Cell_A recorded at room temperature from (A) neutron
 708 radiography (transmission contrasts), (B) slice of the reconstructed 3D stack obtained by neutron
 709 tomography (absorption contrasts), (C) result of the segmentation process performed on the slice shown
 710 in (B), and (D) volume rendering from the segmentation process.

711 **Figure 5.** Typical image of the cycled ^6Li -Li Cell_A recorded at room temperature from (A)
 712 synchrotron X-ray tomography imaging, (B) the segmented slice and (C) volume rendering from the
 713 segmentation process.

714 **Figure 6.** Typical image of the cycled ^6Li -Li Cell_A recorded at room temperature from (A) laboratory
 715 X-ray tomography imaging, (B) segmented slice and (C) volume rendering from the segmentation
 716 process.

717

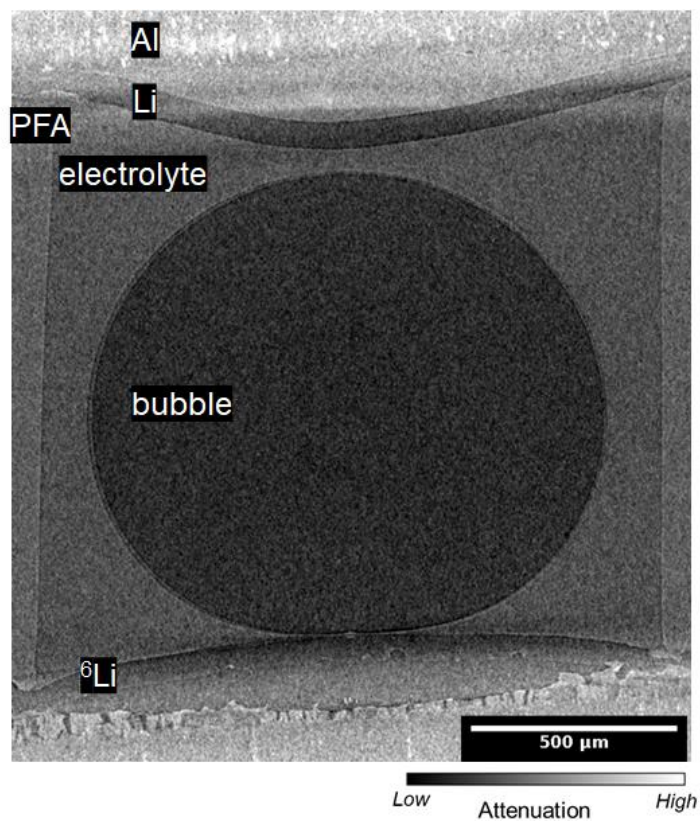
718

719

720

721

722 12 Figures



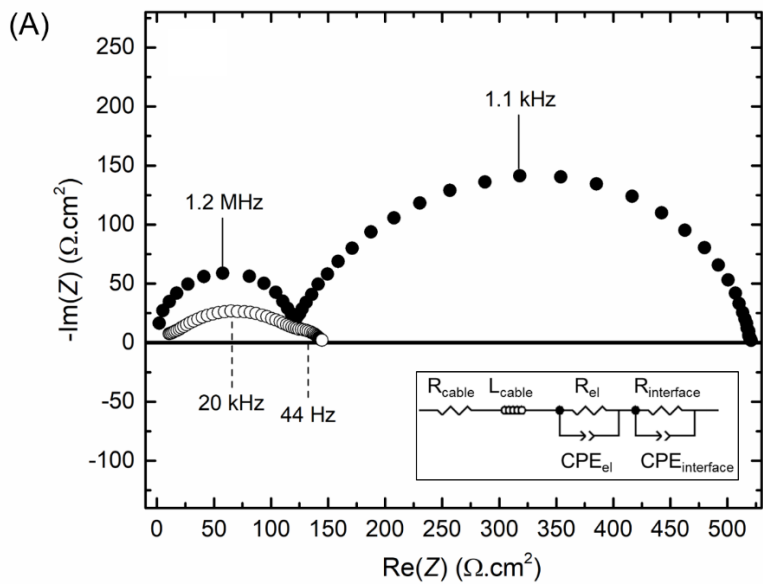
723

724 **Figure 1.**

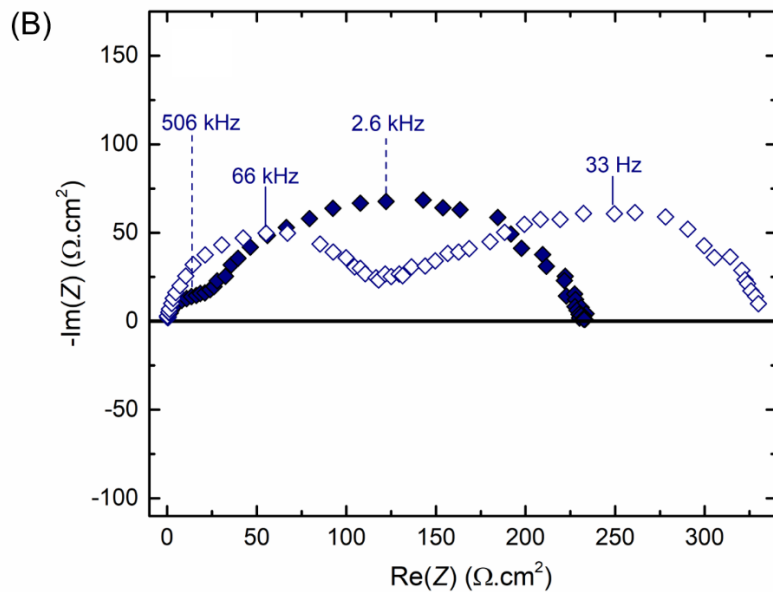
725

726

727

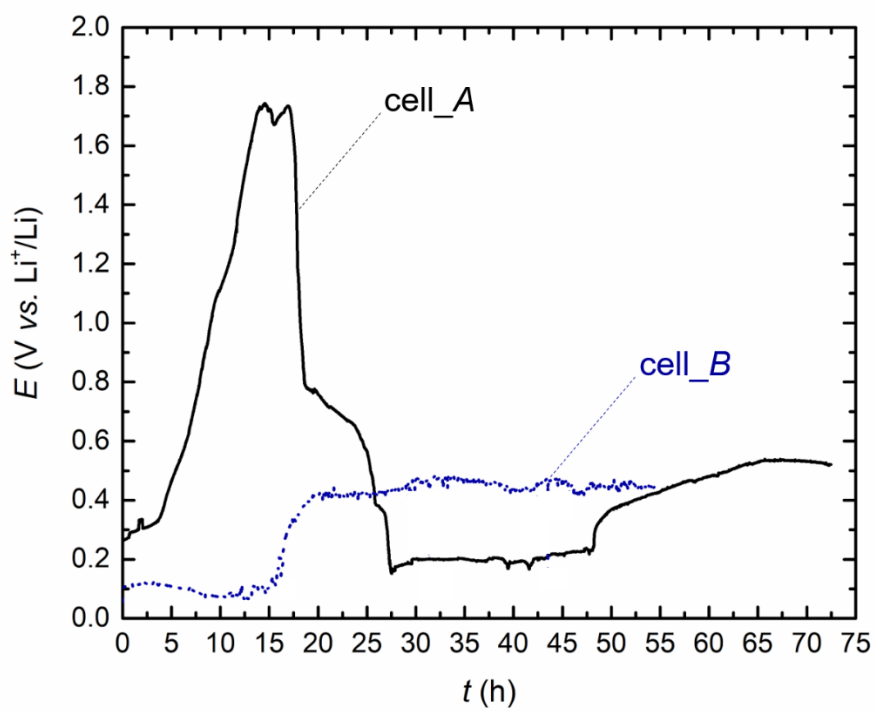


728



729

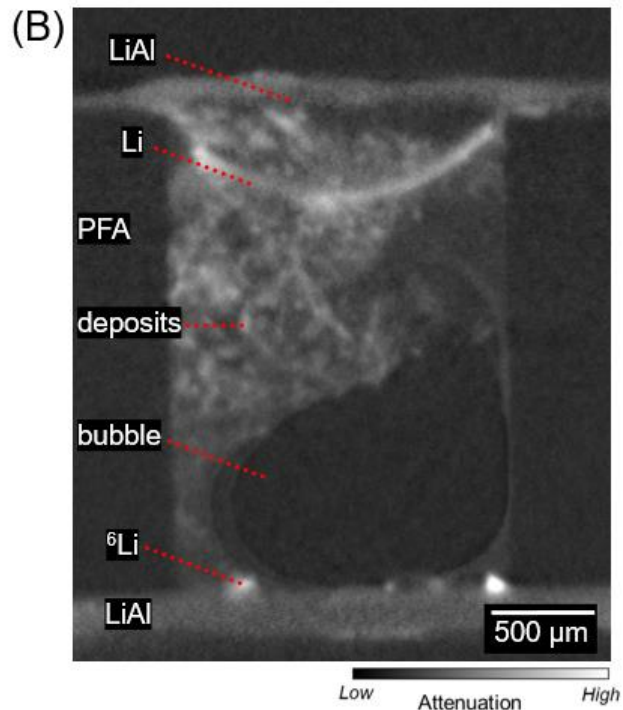
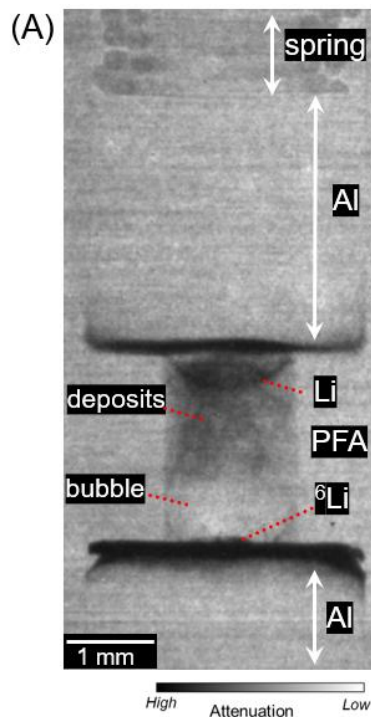
730 **Figure 2.**



731

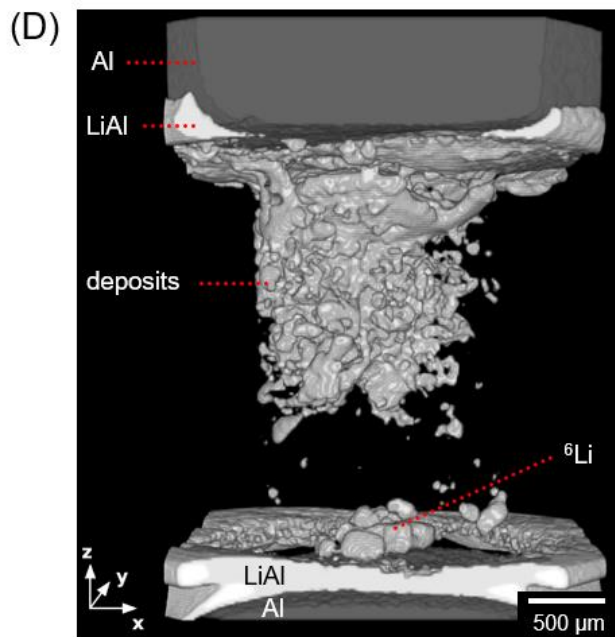
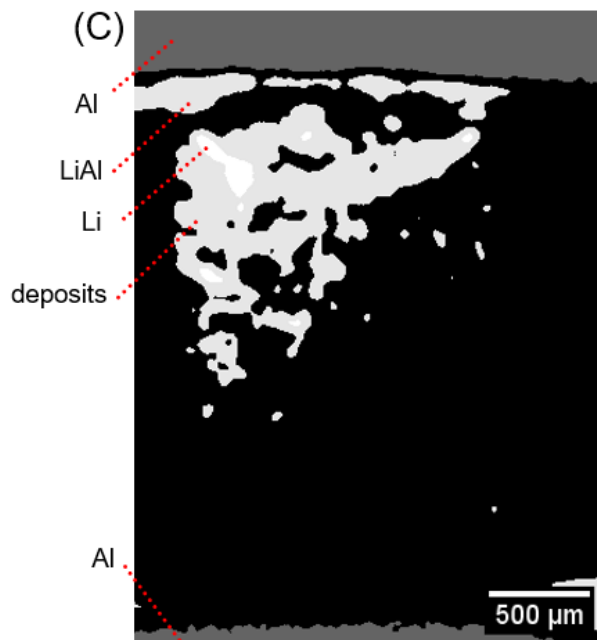
732 **Figure 3.**

733



734

735



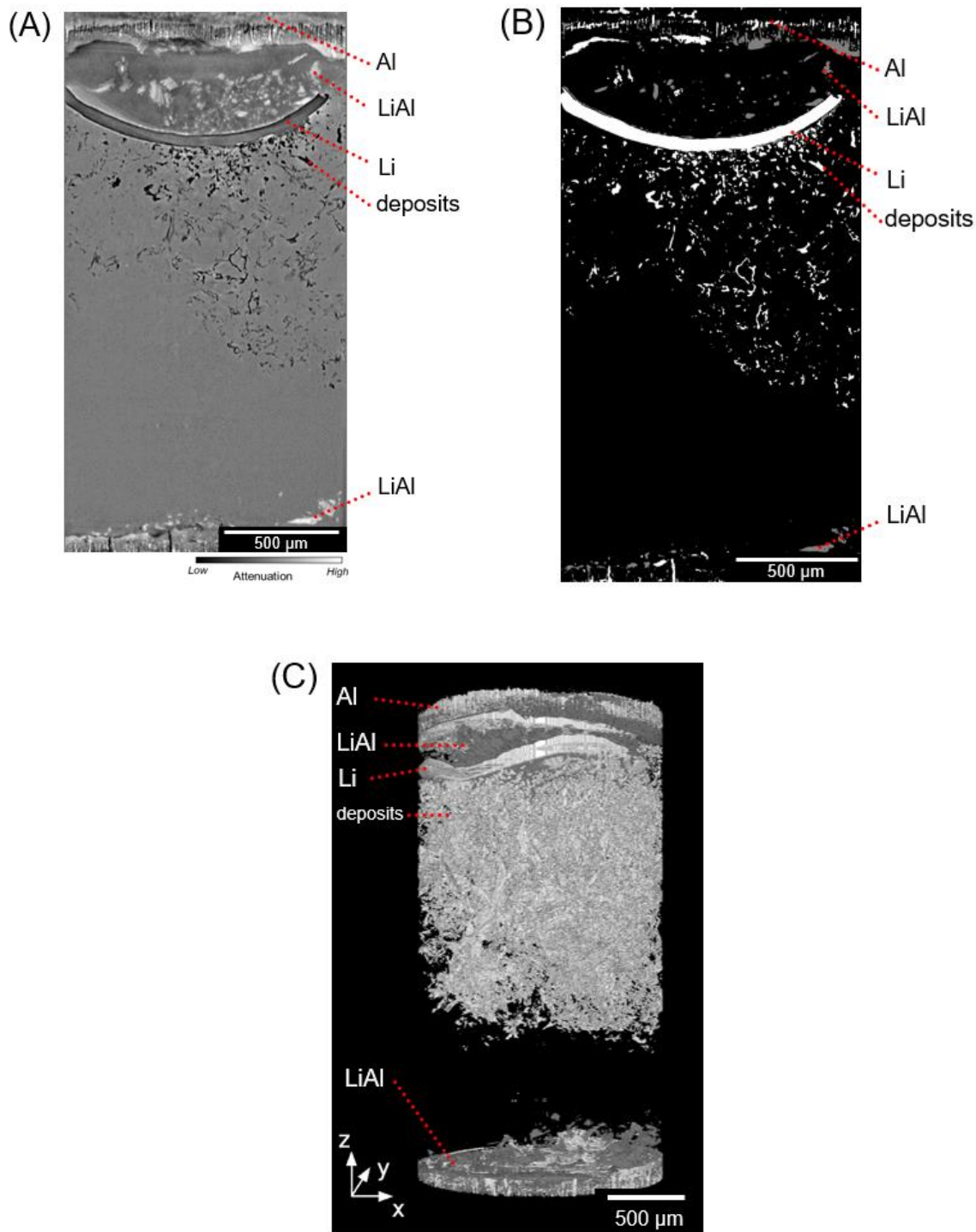
736

737 **Figure 4.**

738

739

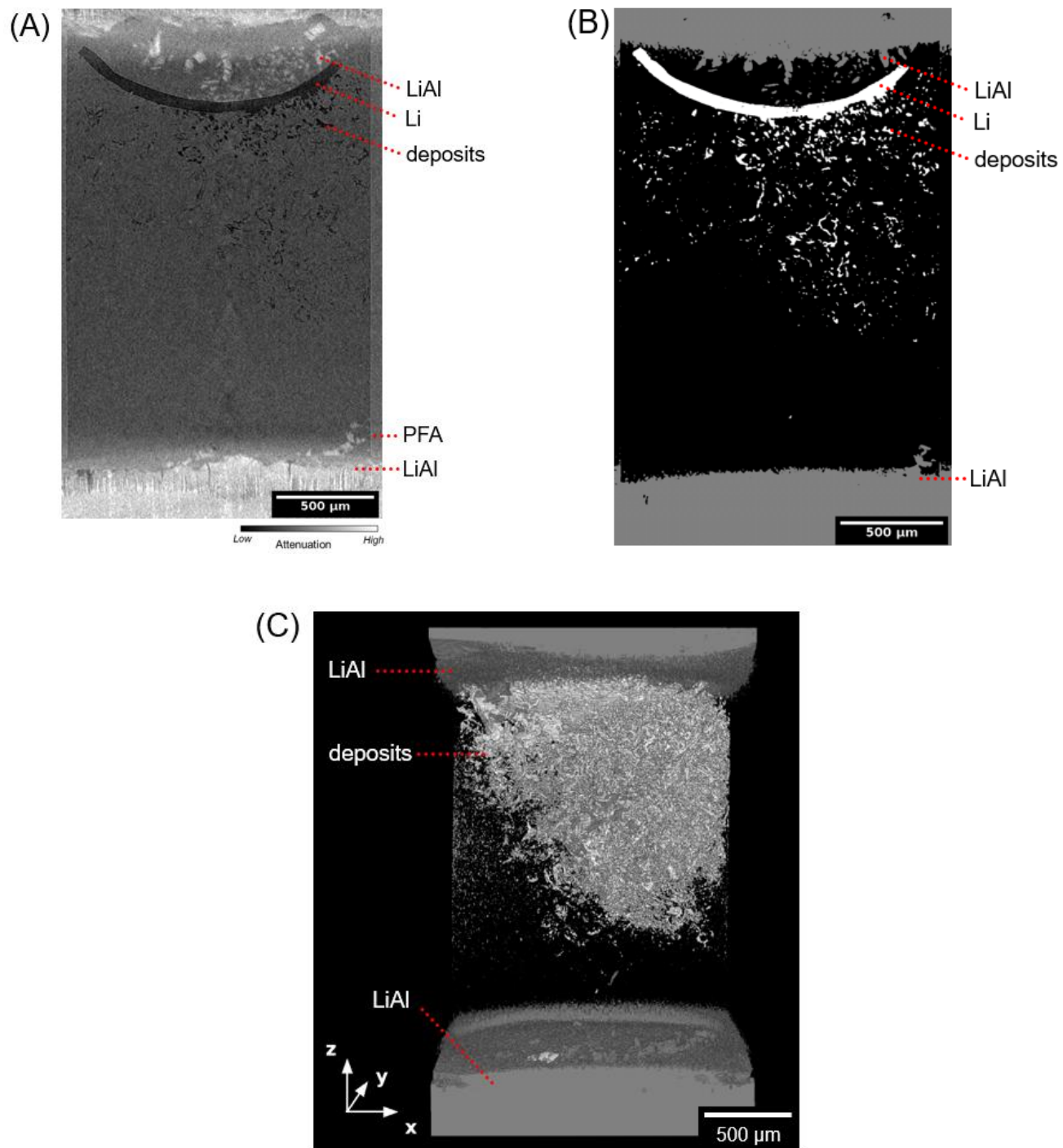
740



741
742

743
744 **Figure 5.**

745
746
747



748

749

750

751 **Figure 6.**